Accessing the full spectrum of corrosion behaviour of tempered type 420 stainless steel

Yiqi Zhou[1] (iD) | **Dirk Lars Engelberg[1,2]** (iD)

[1]Department of Materials, Corrosion & Protection Centre, The University of Manchester, Manchester, UK

[2]Materials Performance Centre, The University of Manchester, Manchester, UK

Correspondence
Yiqi Zhou, Department of Materials, Corrosion & Protection Centre, The University of Manchester, Manchester M13 9PL, UK.
Email: Yiqi.Zhou@manchester.ac.uk

Abstract

Bipolar electrochemistry produces a linear potential gradient between two feeder electrodes, providing access to the full spectrum of anodic-to-cathodic electrochemical behaviour. A type 420 martensitic stainless steel has been used to investigate microstructure evolution and corrosion behaviour with application of different tempering heat treatments. Tempering treatments at 250°C, 400°C and 700°C revealed the occurrence of pitting corrosion, with treatments at 550°C resulting in general and intergranular corrosion. $Cr_{23}C_6$ was present in all tempering conditions, with Cr_7C_3 and CrC only observed for tempering at 550°C. The 250°C tempering treatment had the highest corrosion resistance with a hardness value much higher than 500 HV.

KEYWORDS
bipolar electrochemistry, chromium carbides, heat treatment, intergranular corrosion, martensitic stainless steel, pitting corrosion

1 | INTRODUCTION

Martensitic stainless steel combines excellent wear resistance with hardness and strength. Typical applications include steam generator parts, food processing and mixer blades, cutlery and surgical instruments.[1–3] To produce the martensitic microstructure, type 420 ferritic stainless steel is first annealed at the austenitisation temperature of 950–1050°C, followed by rapid quenching.[4–7] Different austenitisation temperatures, holding times, quench rates and tempering treatments affect the microstructure condition, corrosion behaviour and mechanical properties.[8–11] The subsequent tempering treatments influence the formation of chromium carbides, typically nucleating from M_3C to M_7C_3 and then transforming into $M_{23}C_6$.[12–14] These chromium carbides influence the hardness.[15] The tempering process directly affects the hardness and volume of retained austenite, resulting in a range of tensile behaviours and fracture properties.[16,17] In parallel, tempering time also influences passive film properties, which then, in turn, can affect the corrosion resistance.[18,19]

Martensitic stainless steel is susceptible to localised corrosion in chloride-containing marine environments.[20,21] Pitting corrosion arises from a localised breakdown of the passive film,[22,23] with pits nucleating at microstructure inhomogeneities, such as Cr-depleted regions.[24,25] Pitting corrosion undergoes three stages, from (i) pit nucleation, (ii) metastable pit growth, to (iii) stable pit growth.[26,27] The metastable pit growth often results in pits with lacy covers, which are able to maintain a high concentration of Cl⁻ and a lowpH electrolyte within occluded pit cavities.[28,29] Stable pit growth is associated with a critical electrochemical potential (E_{pit}) or a critical pitting temperature,[30,31] and stable pits generally have a larger pit volume, with the pit depth acting as the diffusion barrier.[32,33]

Bipolar electrochemistry has now become accessible for corrosion testing and screening, featuring a noncontact experimental setup, by in parallel being able to observe the full corrosion response during one single experiment.[34–36] A linear potential gradient is established along the interface of the electrolyte and bipolar electrode (BPE); as a result, both anodic and cathodic reactions are simultaneously occurring along the BPE.[34–37] The potential and current distributions on the BPE were determined by a segmented array BPE, with the bipolar corrosion behaviour compared to the three electrode potentiodynamic and potentiostatic polarisation test.[38] Bipolar electrochemistry has now morphed into a powerful corrosion screening method, providing even access to pitting corrosion kinetics of grade 2205 duplex stainless steel at room temperature.[39] The effect of the duplex stainless steel microstructure in the solution annealed condition was also assessed using the bipolar electrochemistry technique,[40] with examples of brass dezincification and assessment of the galvanic corrosion of dissimilar stainless steel microstructures also explored.[41,42]

This study describes the application of bipolar electrochemistry to assess the effect of tempering treatments on the corrosion behaviour and mechanical property of type 420 stainless steel. The corrosion behaviour determined from three-electrode potentiodynamic polarisation tests was compared with results obtained from bipolar electrochemistry experiments.

2 | MATERIALS AND METHODS

A type 420 ferritic stainless steel with the composition (wt %) of 13.7 Cr, 0.46 C, 0.47 Si, 0.39 Mn and (Bal.) Fe was used in this study. A CWF laboratory chamber furnace was used for heat treatment; the stainless steel samples were first austenitised at 950°C for 1 h, followed by water quenching; the samples were then tempered at 250°C, 400°C, 550°C or 700°C for 1 h, followed by cooling in air. Five different microstructures were tested, with the sample labelled 950°C indicating the quenched, martensitic microstructure without any tempering treatment.

For all bipolar electrochemistry experiments, the BPEs had dimensions of $30 \times 10 \times 1.2\ mm^3$ (length × width × thickness). The BPE samples were mounted in Araldite resin and then prepared by grinding to 1200 grit. For the three-electrode potentiodynamic polarisation test, the samples were cut into $25 \times 25 \times 1.2\ mm^3$ and then well ground to 1200 grit. For the electron backscatter diffraction (EBSD) analysis, the sample was further ground to 4000 grit and polished to a 0.25 μm diamond paste finish, followed by fine polishing with OPS colloidal silica. Microhardness tests were carried out with a Buehler Micromet Tester using an applied load of 4.903 N ($HV_{0.5}$). The mean of five hardness measurements is reported, with the error bars describing the standard deviation of these measurements.

For the three-electrode potentiodynamic polarisation test, the samples were tested in an AVESTA cell at room temperature in a 0.1 M HCl solution. A platinum electrode and an SCE reference electrode were used, in combination with a CS2350 Bipotentiostat and CS Studio 5 software to obtain potentiodynamic polarisation curves. The open-circuit potential (OCP) was measured for 10 min, followed by potentiodynamic polarisation tests from $-200\ mV_{OCP}$ to in excess of $+1500\ mV_{OCP}$ at a scan rate of 1 mV/s. For the bipolar electrochemistry and potentiodynamic polarisation tests, the electrolyte was not deaerated.

Figure 1a shows the bipolar electrochemistry setup. A voltage of 10 V was applied on the feeder electrodes, with the distance between the feeder electrodes set to 60 mm. The BPE was located right in the centre between both feeder electrodes, with each platinum feeder electrode having a surface area of 4 cm^2. All experiments were conducted in 0.1 M HCl with a volume of 200 ml for the
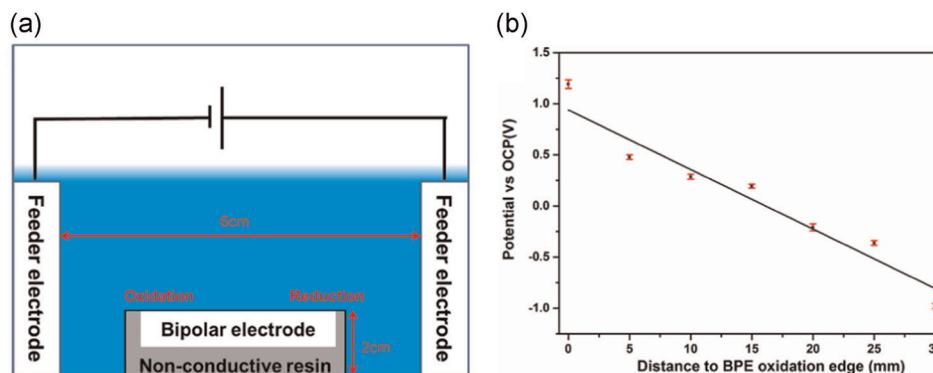

FIGURE 1 (a) Schematic diagram of the bipolar electrochemistry setup with (b) the potential distribution measured along the bipolar electrode (BPE)

duration of 5 min. All bipolar tests were repeated three times. Figure 1b shows the mean potential distribution along the BPE over a timeframe of 600 s. A linear trend line was used to approximate all measured points, with the setup of the potential measurement introduced before.[39]

After completing the bipolar experiment, the BPE was placed in an ultrasonic bath for 600 s to break and remove lacy pit covers, and then cleaned with soap water and dried in hot air. A Keyence VK-200K laser confocal microscope was used to measure the corrosion morphology. All regions had a width of 4 mm, with the overall length of corroded sites depending on the pit-covered length on the BPE. A Zeiss Sigma VP FEG-SEM was used for energy-dispersive X-ray (EDX) analysis from Aztec software at 20 kV. A Tescan Mira 3 LC FEG-SEM was used to acquire scanning electron microscopy (SEM) and EBSD images. For the EBSD, the step size was 110 nm for the microstructure analysis of the matrix and 3 nm for the chromium carbide detection at 15 kV.

3 | RESULTS AND DISCUSSION

The microstructure under conditions of heat-treated type 420 were first characterised. These were then assessed using three-electrode potentiodynamic tests and compared with

the results obtained via bipolar electrochemistry. The corrosion response is then ranked in relation to the microstructures present, allowing differences in corrosion response to be identified for optimising associated tempering treatments for this material.

3.1 | Microstructure characterisation

Figure 2 shows the EBSD images of the different tempering treatments, with the same scale bar for all images. No reverted austenite is present in the quenched microstructure, as no Ni is present in our type 420 material.[43] To support this observation, a prior austenite boundary is outlined in Figure 2a, with the martensitic regions inside the prior austenite grain all having similar grain orientations.

Both retained austenite and martensitic pack sizes changes were with applied tempering treatments. The average area of retained austenite is 18 μm^2 after quenching, 12 μm^2 after tempering at 250°C and 5–7 μm^2 after tempering at 400°C, 550°C and 700°C. The average diameter of lath martensitic regions is 1.7 μm without tempering treatments. Both the retained austenite and martensitic size, in general, decreased with higher tempering temperatures. The grain size can influence pitting corrosion; a fine grain size reduces the metastable pit nucleation, but increases the probability of
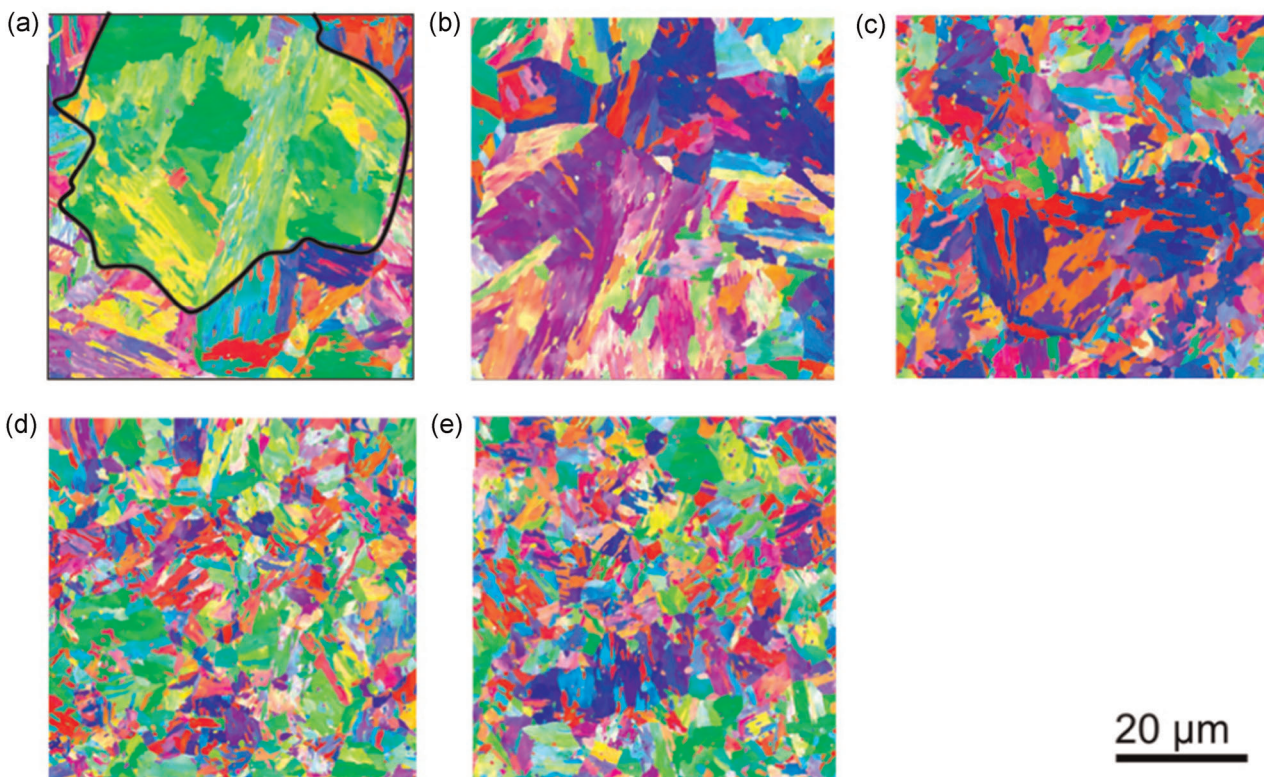

FIGURE 2 Electron backscatter diffraction images of type 420 (a) without tempering treatment and after tempering at (b) 250°C, (c) 400°C, (d) 550°C and (e) 700°C

TABLE 1 Database with crystallographic parameters for EBSD phase identification

Phase	a (Å)	b (Å)	c (Å)	Alpha	Beta	Gamma	Space group	Phase
Fe3C	5.11	6.78	4.54	90.00°	90.00°	90.00°	62	BCT
Cr_3C	5.12	6.80	4.58	90.00°	90.00°	90.00°	62	
Cr_3C_2	5.53	11.49	2.83	90.00°	90.00°	90.00°	62	
Cr_7C_3	4.53	7.01	12.14	90.00°	90.00°	90.00°	62	
$Cr_{23}C_6$	10.66	10.66	10.66	90.00°	90.00°	90.00°	225	FCC
CrC	4.03	4.03	4.03	90.00°	90.00°	90.00°	225	

Abbreviations: BCT, body-centred tetragonal; EBSD, electron backscatter diffraction; FCC, face-centred cubic.
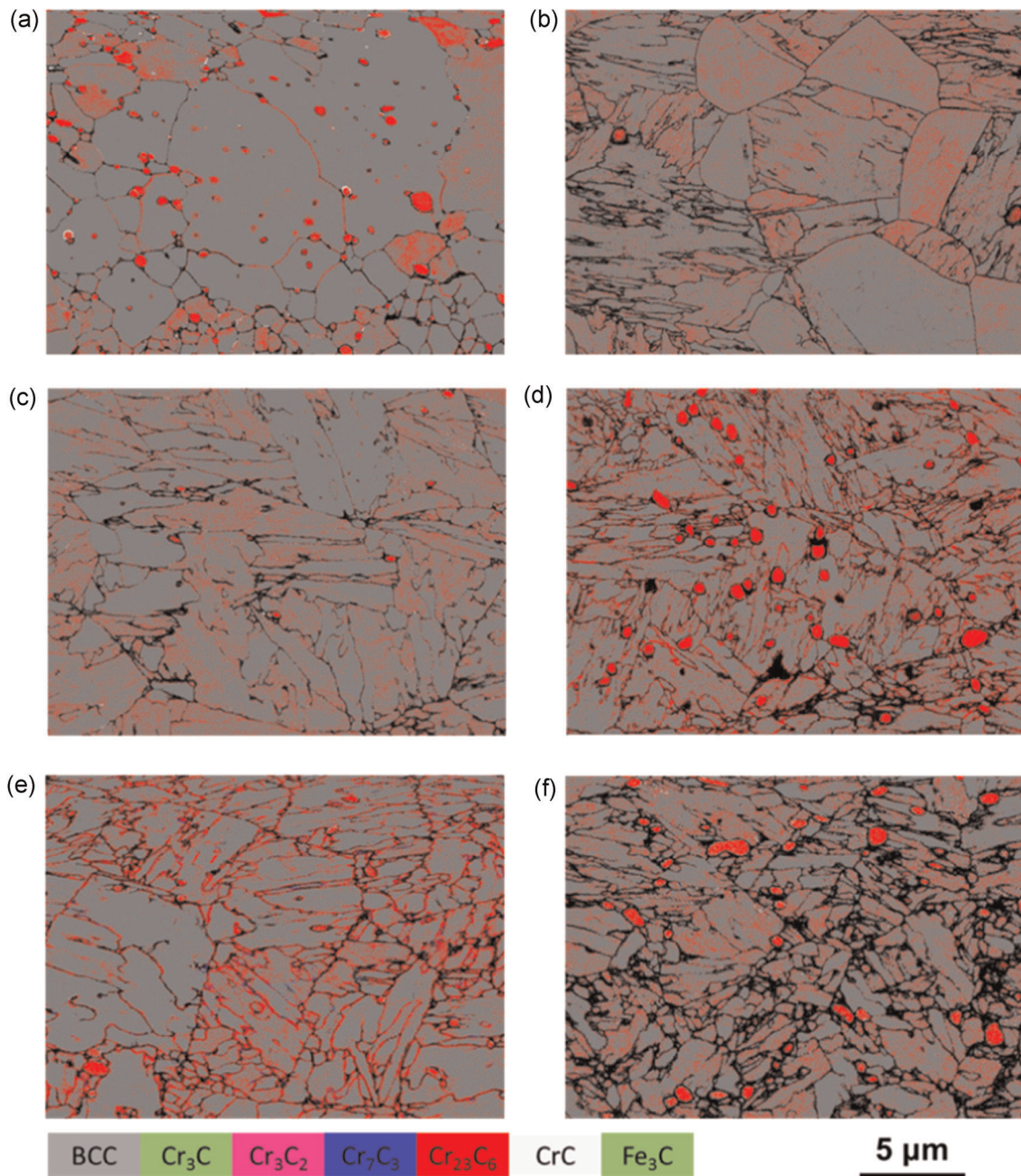

FIGURE 3 Electron backscatter diffraction maps of chromium carbides in the (a) as-received ferritic stainless steel, and after austenitisation and water quenching in (b), and tempering at (c) 250°C, (d) 400°C, (e) 550°C and (f) 700°C
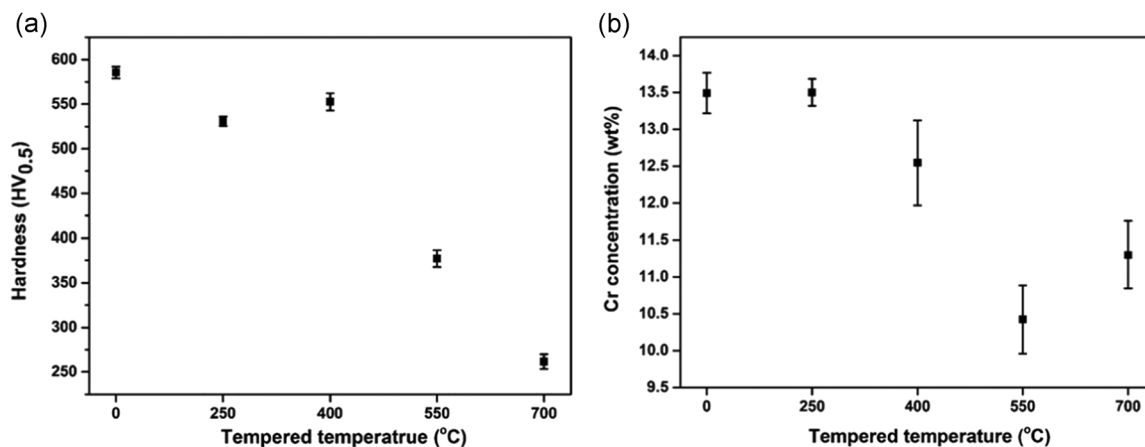
FIGURE 4 (a) Hardness and (b) Cr concentration evolution with different tempering temperatures
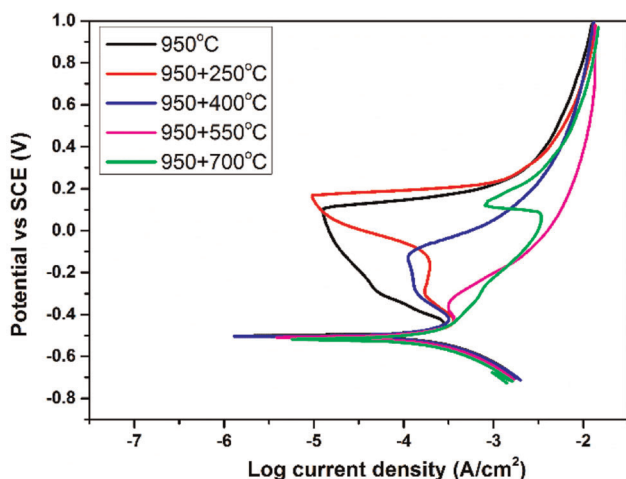

FIGURE 5 Standard three-electrode potentiodynamic polarisation curves for all heat-treated samples in 0.1 M HCl solution at room temperature (the material labelled 950°C is the quenched/martensitic microstructure before tempering treatment)

forming a stable pit.[44] Retained austenite can improve the corrosion resistance of the martensitic stainless steel.[25]

To identify different types of chromium carbides, EBSD analyses with associated crystallographic parameters were carried out. The identification of different carbides by EBSD is typically not unanimous, as some of the carbides have similar lattice parameters, summarised in Table 1. These parameters were obtained from the Inorganic Crystal Structure Database (ICSD) and Aztec software used for EBSD phase acquisition. The scale bar is the same for all EBSD images.

Figure 3 shows as-received type 420 stainless steel before the 950°C austenitisation treatment, showing a discrete distribution of $Cr_{23}C_6$ at the surface. The as-received ferritic microstructure was assessed and investigated in an earlier study.[45]

Figure 3b shows that after the austenitisation treatment at 950°C, most carbides were dissolved into the matrix. After tempering at 250°C was carried out, some $Cr_{23}C_6$ was found at grain boundaries, possibly remnants from the as-received microstructure. After tempering at 400°C, larger sizes and more $Cr_{23}C_6$ were present, and after tempering at 550°C, more carbides were found. The sample tempered at 550°C also had CrC and Cr_7C_3, as well as $Cr_{23}C_6$ at grain boundaries; this is possibly the reason why intergranular corrosion was observed under potentiodynamic polarisation and bipolar electrochemistry testing. However, only a small fraction of CrC and Cr_7C_3 was observed, as most of these carbides transformed into the stable $Cr_{23}C_6$.[10,12,46,47]

After tempering at 700°C, only $Cr_{23}C_6$ was observed. The Cr diffusion rate is increased at high temperatures, which allows the formation of large-sized chromium carbides.[48] Chromium carbides prefer to precipitate at grain boundaries as there is also typically a higher diffusion rate and the precipitation is energetically more favoured.[49] Pitting corrosion was reported to arise next to the chromium carbide precipitates.[45]

3.2 | Hardness and chemistry

The hardness values of all type 420 samples are summarised in Figure 4a. The martensitic microstructure and the samples heat treated at 250°C and 400°C had similar hardness values of ≈550–600 $HV_{0.5}$. The hardness slightly decreased after tempering at 250°C, possibly due to the smaller retained austenite grain size,[50] and then slightly increased in hardness after tempering at 400°C, as new carbides formed,

TABLE 2 Pitting potential, corrosion potential and E_{pit} obtained after different tempering treatments of stainless steel after polarisation in 0.1 M HCl electrolyte at room temperature

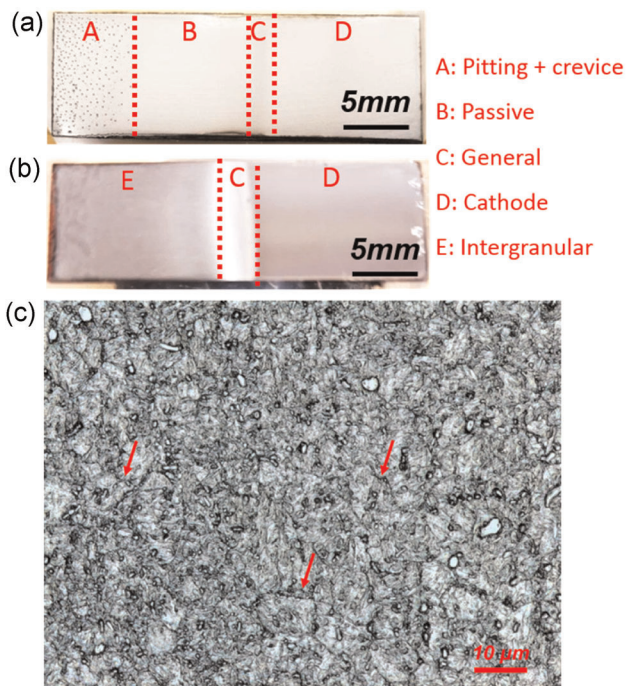| Temperature (°C)	E_{corr} (V_{SCE})	$E_{ave.\ corr}$ (V_{SCE})	E_{pit} (V_{SCE})	$E_{ave.\ pit}$ (V_{SCE})
950	−0.495	−0.501 ± 0.006	0.10	0.11 ± 0.01
	−0.505		0.10	
	−0.505		0.12	
950 + 250	−0.516	−0.513 ± 0.003	0.18	0.17 ± 0.01
	−0.513		0.17	
	−0.511		0.16	
950 + 400	−0.517	−0.515 ± 0.002	−0.04	−0.03 ± 0.01
	−0.515		−0.03	
	−0.513		−0.03	
950 + 550	−0.514	−0.510 ± 0.004	–	–
	−0.510		–	
	−0.506		–	
950 + 700	−0.528	−0.527 ± 0.001	0.10	0.12 ± 0.02
	−0.527		0.12	
	−0.527		0.13	

FIGURE 6 Images of type 420 tempered at (a) 400°C and (b,c) 550°C after bipolar corrosion testing with 5-min exposure. The left side is the oxidation edge, with the dashed lines indicating different corrosion regions. (c) Micrograph of the corroded region with the arrows highlighting intergranular attack

often referred to a secondary hardening effect.[51] The hardness values then reduced to 370 and 250 HV$_{0.5}$ after tempering at 550°C and 700°C. At 550°C, the hardness is reduced as large numbers of chromium

carbides are formed. The hardness of the martensitic stainless steel was related to the size and distribution of the chromium carbides.[15,52]

Figure 4b shows the concentration of chromium in the matrix, which is the average of 10 points measured by EDX, with the error bar based on the standard deviation of these measurements. The critical concentration of chromium to form a protective passive film is about 12%. At tempering below 400°C, the chromium concentration is >12%, which is certainly enough to form a passive film. After tempering at 550°C, the chromium concentration is down to 10.5%, just at the border, to form a protective passive film, with corrosion then occurring at the chromium depletion region, resulting in intergranular corrosion. After tempering at 700°C, the chromium is again ≈11.5%, with localised corrosion occurring adjacent to chromium carbides, resulting in pit nucleation.

3.3 | Potentiodynamic polarisation

Potentiodynamic polarisation curves as a function of tempering temperature are all summarised in Figure 5. Each test was carried out three times, and the results are consistent and reproducible. The OCP for all tested samples was around −0.5 V$_{SCE}$.

The E_{pit} for the MSS 420 without tempering (950°C) is around +0.11 V$_{SCE}$. After tempering at 250°C, the E_{pit} increased to +0.17 V$_{SCE}$, with two distinct active–passive transitions apparent within the passive region. The first transition is typically associated with passivation
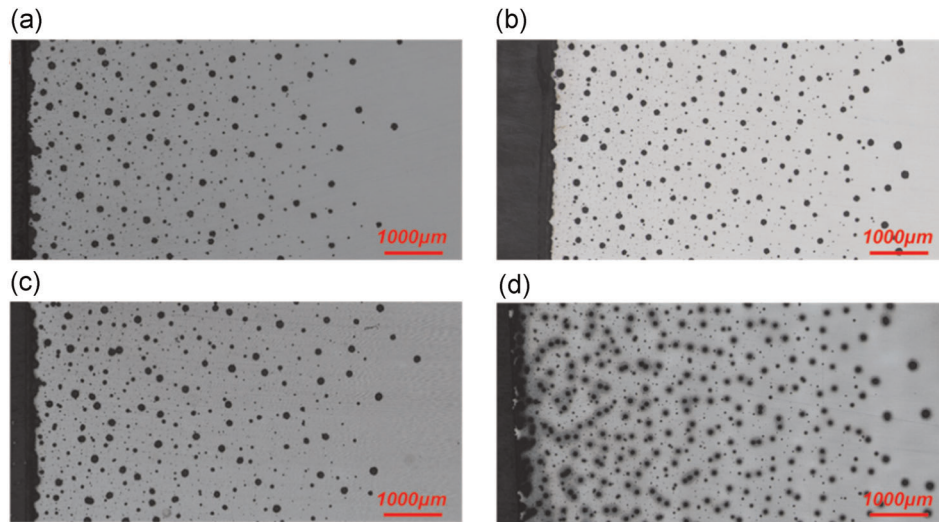
FIGURE 7 Optical images of the pit-covered region after bipolar electrochemistry experiments under different tempering temperatures: (a) no tempering, (b) 250°C, (c) 400°C and (d) 700°C
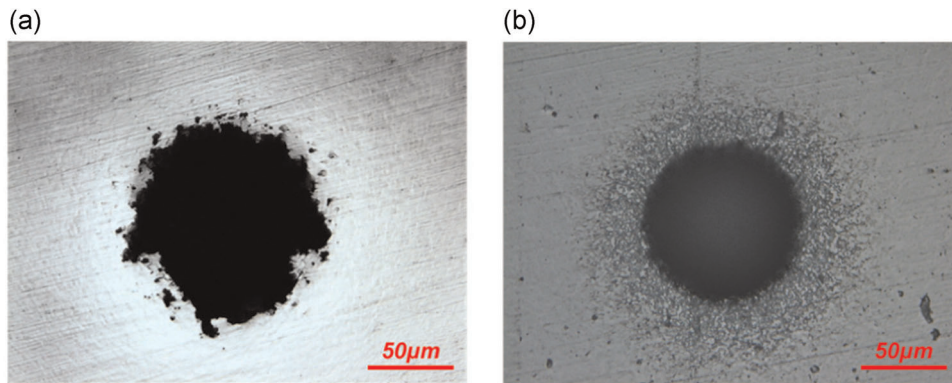

FIGURE 8 Optical images of single pits on the bipolar electrode after tempering treatment at (a) 250°C and (b) 700°C

reactions in Cr-containing stainless steels, with the second transition possibly related to passive film formation around or at Cr-depleted regions.[53] After tempering at 400°C, E_{pit} reduced to −0.03 V_{SCE}, and after tempering at 550°C, no pitting corrosion was observed from the polarisation curves. Posttest examination of microstructures showed the presence of chromium carbides at grain boundaries, resulting in intergranular corrosion.[46,54] After tempering treatments at 700°C, E_{pit} increased to +0.12 V_{SCE}. However, no obvious passive region was formed as the current density remained >0.1 mA/cm^2 at all times, with pits confirmed to be present during post-exposure observations. All results extracted from our polarisation curves are presented in Table 2. Interestingly, all polarisation curves showed distinct materials behaviour, as the tempering treatment affected the properties of the passive film.[18]

3.4 | Bipolar electrochemistry

All tempering-treated stainless steel microstructures were then corrosion-tested with the bipolar electrochemistry experimental setup. Figure 6a shows the corrosion response of the 400°C and 550°C tempering-treated microstructures, with different responses at the surface regions separated by red dashed lines. The left sides of both images display the oxidation edge (anodic side), with the reduction edge (cathodic side) located at the opposite edge. From the oxidation edge to the reduction edge, an anodic trans-passive, active/passive, followed by a cathodic polarisation response is present, with part of the surface corroded and part of the surface showing no corrosion attack at all.
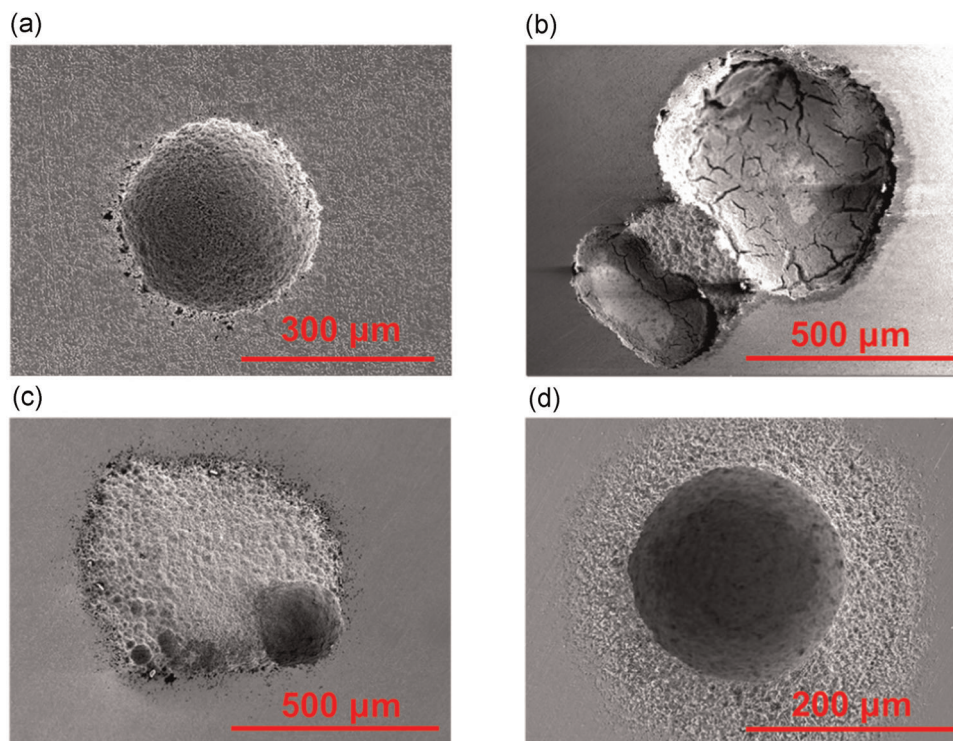
FIGURE 9 Different pit morphologies after potentiodynamic polarisation testing for (a), (b,c) tempering below 400°C and (d) pit measured after a tempering treatment at 700°C

Crevice corrosion at the interface to the resin is typically present along the length of the BPE, starting from the oxidation edge. The length of corroded crevices (and pits) along the sample can be used to evaluate and rank microstructure behaviour. The observed crevices were longer than pit corrosion-containing regions, supporting a lower nucleation potential for crevices compared with pits. After tempering at 550°C, crevice corrosion, general corrosion and a cathodic area were found, shown in Figure 6b, with the 400°C heat-treated samples also showing a passive region. A region containing both general and intergranular corrosion is shown in Figure 6c.

Figure 7 shows a summary of pit-covered regions of the BPEs with different tempering treatments. No pitting was observed in the 550°C tempering-treated sample, supporting the observations made in Figure 5. The length of the pit-covered region was different depending on the tempering-treated microstructure, indicating variations in pitting attack and associated critical pitting potentials. Differences in pit sizes and nucleated pit frequencies are also apparent in Figure 7, with most pits observed after tempering at 700°C. Closer observation also shows grain boundary etch attack in all samples shown in Figure 7. Tempering treatments below 400°C had remnants of lacy metal covers adjacent to pits, with predominantly larger, open pits observed in the 700°C tempering-treated sample (Figure 8). This indicates that larger sized pits are stable pits

and the smaller pits are most likely metastable pits. Corrosion attack surrounding the larger pits at high applied potential was found after tempering at 700°C.

Figure 8a shows a pit in 250°C-treated sample. The pit shape is circular, but the edge is not smooth, with the lacy cover partly collapsed into the pit due to the ultrasonic bath treatment before surface inspection. Figure 8b shows a pit of a sample tempered at 700°C, having a circular pit mouth and no lacy cover remnants. The rough, attacked surface surrounding the pit is shown here, which most likely derives from pit electrolyte effluent diffusing out of the pit cavity.[45]

Comparison of Figure 8 with Figure 5 indicates that a passive film is formed in tempering-treated samples at 400°C and below, with the passive layer resulting in lacy cover pits. Both the three-electrode potentiodynamic polarisation tests and the bipolar electrochemistry tests show similar results, with no pitting found in microstructures tempered at 550°C. Pits nucleated in microstructures tempered at 700°C have a different morphology compared with the other microstructures.

3.5 | Microstructure observation after corrosion testing

Four different pit morphologies were determined after three-electrode potentiodynamic polarisation testing. All
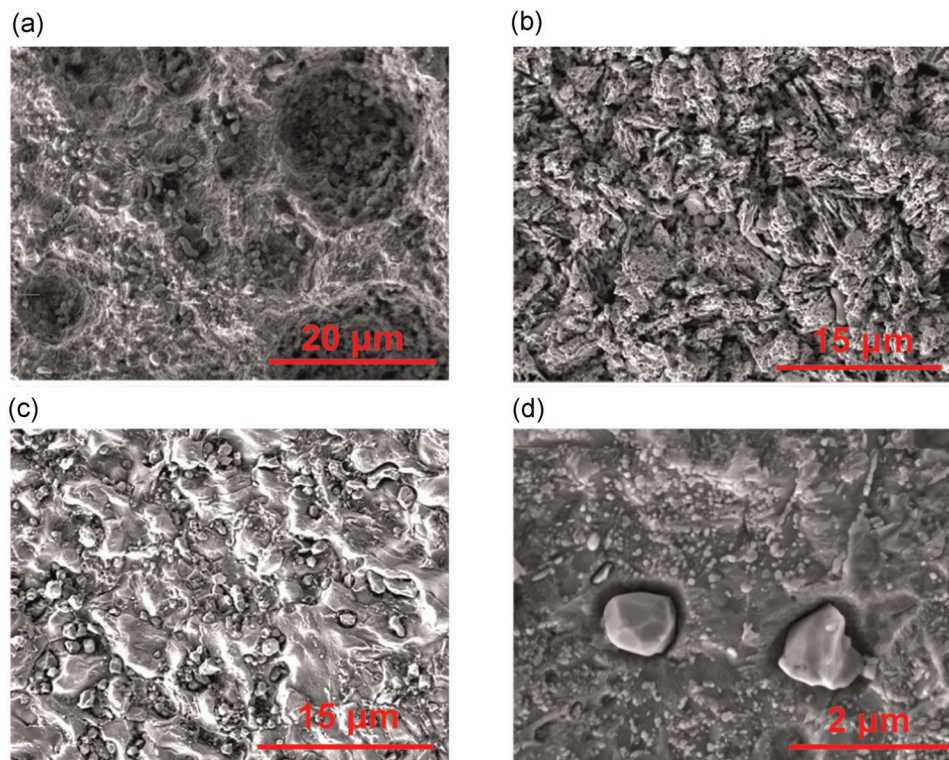
FIGURE 10 Area with corrosion surrounding pits after potentiodynamic polarisation testing for (a) tempering at 250°C and (b) intergranular corrosion for the microstructure tempered at 550°C. Corrosion in the circumference after (c) tempering at 700°C and at (d) higher magnification

larger-sized pits were open pits, possibly related to the high overpotential obtained towards the end of these tests. Figure 9a shows a circular cross-section pit, with a clean pit bottom and a diameter $\approx$300 μm. Some chromium carbides stand proud of the matrix, indicating the higher corrosion resistance of these carbides. Figure 9b shows two elliptical pits; the surface area between the two pits is roughened, caused by general corrosion from pit effluent. The bigger pit has a diameter $\approx$500 μm with corrosion products still inside the pit; from the EDX analysis, it was found that the corrosion product has high concentrations of Cr, O and Cl, and a lower Fe content.

During pit growth, Cr and Fe dissolve and react with Cl ions and O_2, under the formation of oxides/oxyhydroxides and chlorides.[55] The corrosion rate and pit morphology are changed by the porosity of the corrosion product.[56,57] Figure 9c shows a circular pit with a diameter of 200 μm, with the diameter of the surrounding region showing general corrosion of >500 μm. When type 420 was tempered at 700°C, only one type of pit was found, shown in Figure 9d, a spherical shape of about 200 μm diameter and a circular pit ring with a diameter of 300 μm surrounding the pit.

Figure 10a shows an SEM image of the circumference of the pit of the 250°C tempering-treated microstructure. The chromium carbides are clearly seen alongside some cavities,
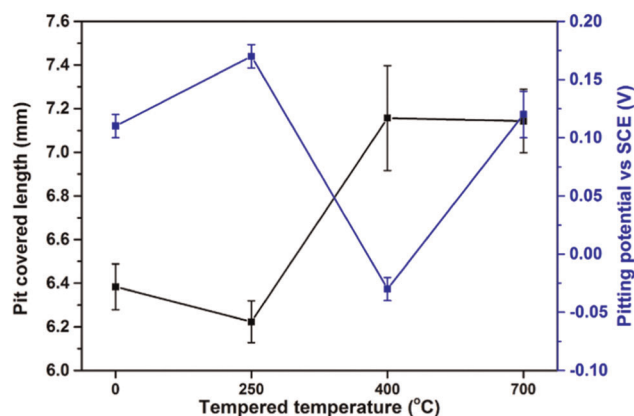

FIGURE 11 Length of the pit-covered region on the bipolar electrode and E_{pit} measured from the three-electrode polarisation test

which are possibly associated with metastable pits. Figure 10b shows the intergranular corroded microstructure after tempering at 550°C. Figure 10c shows the surface of the inner part of the corroded pit circumference after tempering at 700°C, with ellipsoid chromium carbides standing proud of the surface. A higher magnification image of the pit ring is shown in Figure 10d. Linked to Figure 2, when tempering was carried out at 700°C, the high current density after
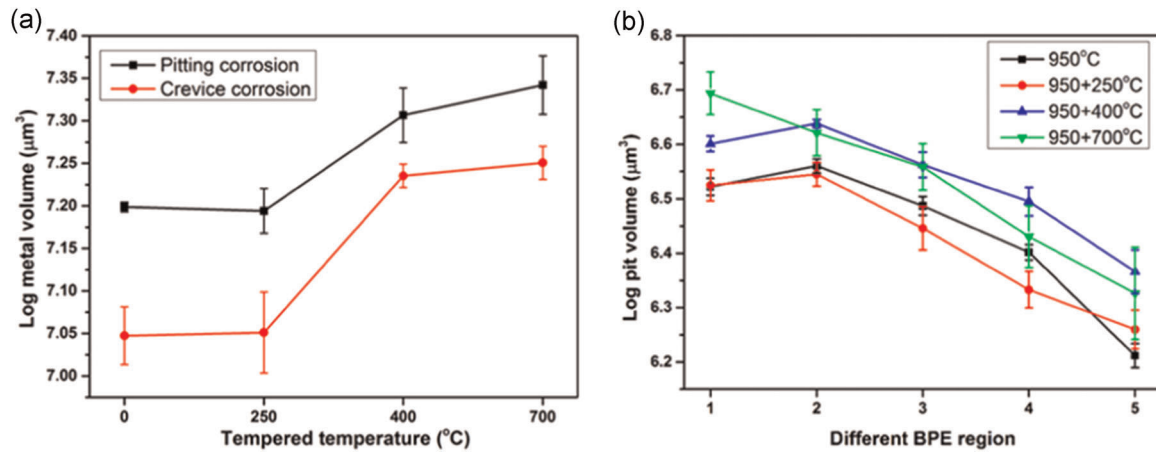
FIGURE 12 (a) Overall pitting and crevice corrosion volume on the bipolar electrode (BPE) and (b) pitting corrosion volume along the BPE with different tempering treatments

reaching E_{pit} resulted in selective dissolution of regions surrounding these carbides.[45]

Figure 11 shows the E_{pit} from three-electrode polarisation test and the bipolar pit-covered length on the BPE as a function of the different tempering treatments. A longer pit-covered length indicates a lower pit nucleation potential. From the E_{pit} obtained from the potentiodynamic polarisation test, the corrosion resistance rank is $250°C > 700°C >$ martensitic $\approx 400°C$. From the bipolar test, the rank is $250°C >$ martensitic $> 400°C > 700°C$. After tempering at $700°C$, E_{pit} displays a higher corrosion resistance, but has a longer pit-covered length on the BPE. This is possibly linked to the reduced stability of the passive film on this sample, which, in turn, results in higher E_{pit} due to the applied scan rate (1 mV/s). The bipolar experiment is not affected by scan rates and has no scan rate dependency.

Figure 12a shows the average metal loss with standard deviation from pitting and crevice corrosion in three distinctive samples. The measured corrosion volume on the BPE shows similar tendencies of the different tempering temperatures, with a larger corrosion volume found after the $400°C$ and $700°C$ treatments, and the smallest corrosion volume found for the $250°C$ sample. From the corrosion volume, the corrosion resistance rank is $250°C >$ martensitic $> 400°C \approx 700°C$.

Figure 12b shows the volume of corrosion only from pits along the BPE. The corroded surface was divided into five equal-sized regions, with each region spanning a size of $1 \times 4\,mm^2$ (length × width). Region 1 represents the highest potential close to the oxidation edge, and region 5, located 4–5 mm away from the oxidation edge, represents the lowest applied potential. Due to a linear potential gradient along the BPE, the pitting corrosion volume is reduced from region 1 to region 5. Here, the pit volume slightly

increases from region 1 to region 2, as most of the available current was consumed by the large crevice at the oxidation edge corrosion. The limited availability of current density suppresses the pit growth in region 1. From region 2 to region 5, the pit volume is reduced due to the lower applied potential. The pit volume in each region follows $700°C > 400°C >$ martensitic $> 250°C$, which is similar to the rank of overall localised volume on the BPE. Hence, the pit growth kinetics in all applied potential regions is the lowest after tempering at $250°C$ and the highest after tempering at $700°C$ in all of the assessed regions.

The pitting corrosion resistance determined from bipolar electrochemistry and the three-electrode potentiodynamic polarisation test yields the same rank for tempered type 420 martensitic stainless steel. Unlike the three-electrode potentiodynamic polarisation test, which only offers the critical pitting potential, the advantage of using bipolar electrochemistry for corrosion tests includes access to pit growth kinetics within the different potential regions.

To optimise the corrosion and hardness of type 420 martensitic stainless steel, tempering at $250°C$ is the best choice, resulting in the highest corrosion resistance (high E_{pit} and low pit growth kinetics) and a high hardness value ($>500\,HV_{0.5}$). Tempering at $550°C$ and $700°C$ should be avoided, as the hardness and corrosion resistance are reduced, due to the large number and size of chromium carbides formed.

4 | CONCLUSION

- Bipolar electrochemistry has been used to determine the corrosion behaviour of tempered martensitic type 420 stainless steel.

- Intergranular corrosion arises after tempering treatments at 550°C due to the presence of chromium carbides at grain boundaries.
- The pitting corrosion resistance rank is 250°C > martensitic > 400°C > 700°C, based on the pit volume and pit-covered length.
- $Cr_{23}C_6$ is determined for all the tempering samples, and CrC and Cr_7C_3 are only present for samples tempered at 550°C.

ACKNOWLEDGEMENTS

DATA AVAILABILITY STATEMENT

The data that support the findings of this study are available on request from the corresponding author.

ORCID

Yiqi Zhou http://orcid.org/0000-0001-6513-7460
Dirk Lars Engelberg http://orcid.org/0000-0002-0519-7354

REFERENCES

[1] K. H. Anantha, C. Örnek, S. Ejnermark, A. Medvedeva, J. Sjöström, J. Pan, *J. Electrochem. Soc.* **2017**, *164*, C85.
[2] A. F. Candelaria, C. E. Pinedo, *J. Mater. Sci. Lett.* **2003**, *22*, 1151.
[3] A. Dalmau, C. Richard, A. Igual-Muñoz, *Tribol. Int.* **2018**, *121*, 167.
[4] L. D. Barlow, M. Du Toit, *J. Mater. Eng. Perform* **2012**, *21*, 1327.
[5] C.J. Scheuer, R.A. Fraga, R.P. Cardoso, S.F. Brunatto, in: 21 CBECIMAT - Congr. Bras. Eng. e Ciência Dos Mater., 2014, 5857.
[6] R. Schneider, J. Perko, G. Reithofer, *Mater. Manuf. Process.* **2009**, *24*, 903.
[7] S. K. Berezin, A. A. Shatsov, P. O. Bykova, D. M. Larinin, *Met. Sci. Heat Treat.* **2017**, *59*, 479.
[8] X. Lei, Y. Feng, J. Zhang, A. Fu, C. Yin, D. D. Macdonald, *Electrochim. Acta* **2016**, *191*, 640.
[9] C. García De Andrés, L. F. Álvarez, V. López, J. A. Jiménez, *J. Mater. Sci.* **1998**, *33*, 4095.
[10] A. N. Isfahany, H. Saghafian, G. Borhani, *J. Alloys Compd.* **2011**, *509*, 3931.
[11] K. H. Anantha, C. Örnek, S. Ejnermark, A. Medvedeva, J. Sjöström, J. Pan, *J. Electrochem. Soc.* **2017**, *164*, C810.
[12] S.-Y. Lu, K.-F. Yao, Y.-B. Chen, M.-H. Wang, X.-Y. Ge, *Metall. Mater. Trans. A* **2015**, *46A*, 6090.
[13] C. Köse, R. Kaçar, *Mater. Des.* **2014**, *64*, 221.
[14] C. J. Scheuer, F. Possoli, P. C. Borges, R. P. Cardoso, S. F. Brunatto, *Electrochim. Acta* **2019**, *317*, 70.
[15] S. K. Bonagani, V. Kain, N. Naveen Kumar, H. Donthula, *J. Mater. Eng. Perform.* **2021**, *30*, 2291.
[16] H. Nakagawa, T. Miyazaki, *J. Mater. Sci.* **1999**, *34*, 3901.
[17] E. de Moor, S. Lacroix, A. J. Clarke, J. Penning, J. G. Speer, *Metall. Mater. Trans. A* **2008**, *39*, 2586.
[18] K. Morshed-Behbahani, N. Zakerin, P. Najafisayar, M. Pakshir, *Corros. Sci.*, *183*, 109340.
[19] G. Wei, S. Lu, S. Li, K. Yao, H. Luan, X. Fang, *Corros. Sci.* **2020**, *177*, 108951.
[20] P. D. Krell, S. Li, H. Cong, *Corros. Sci.* **2017**, *122*, 41.
[21] S. Marcelin, N. Pébère, S. Régnier, *J. Electroanal. Chem.* **2015**, *737*, 198.
[22] S. Pahlavan, S. Moazen, I. Taji, K. Saffar, M. Hamrah, M. H. Moayed, S. Mollazadeh Beidokhti, *Corros. Sci.* **2016**, *112*, 233.
[23] S. Frangini, N. De Cristofaro, *Corros. Sci.* **2003**, *45*, 2769.
[24] K. Chandra, V. Kain, R. Tewari, *Corros. Sci.* **2013**, *67*, 118.
[25] S. Y. Lu, K. F. Yao, Y. B. Chen, M. H. Wang, N. Chen, X. Y. Ge, *Corros. Sci.* **2015**, *103*, 95.
[26] S. M. G. Burstein, P. Pistorius, *Corros. Sci.* **1993**, *35*, 57.
[27] G. Meng, Y. Li, Y. Shao, T. Zhang, Y. Wang, F. Wang, *J. Mater. Sci. Technol.* **2014**, *30*, 253.
[28] G. S. Frankel, L. Stockert, F. Hunkeler, H. Boehni, *Corrosion* **1987**, *43*, 429.
[29] J. Srinivasan, R. G. Kelly, *J. Electrochem. Soc.* **2016**, *163*, C768.
[30] N. J. Laycock, *J. Electrochem. Soc.* **1998**, *145*, 2622.
[31] C. J. Semino, P. Pedeferri, G. T. Burstein, T. P. Hoar, *Corros. Sci.* **1979**, *19*, 1069.
[32] J. Srinivasan, M. J. McGrath, R. G. Kelly, *Electrochem. Soc* **2014**, *58*, 1.
[33] N. J. Laycock, R. C. Newman, *Corros. Sci.* **1997**, *39*, 1771.
[34] Y. Zhou, D. L. Engelberg, *Electrochem. Commun.* **2018**, *93*, 158.
[35] S. Munktell, M. Tydén, J. Högström, L. Nyholm, F. Björefors, *Electrochem. Commun.* **2013**, *34*, 274.
[36] N. Pébère, V. Vivier, *ChemElectroChem* **2016**, *3*, 415.
[37] R. M. Crooks, *ChemElectroChem* **2016**, *3*, 357.
[38] Y. Zhou, N. Stevens, D. Engelberg, *Electrochim. Acta* **2021**, *375*, 137668.
[39] Y. Zhou, D. L. Engelberg, *Electrochem. Commun.* **2020**, *117*, 106779.
[40] Y. Zhou, A. Kablan, D. L. Engelberg, *Mater. Charact.* **2020**, *169*, 110605.
[41] Y. Zhou, S. Mahmood, D. Engelberg, *Surf. Interfaces* **2021**, *22*, 100865.
[42] Y. Zhou, J. Qi, D. L. Engelberg, *Electrochem. Commun.* **2021**, *126*, 107023.
[43] Y. Y. Song, X. Y. Li, L. J. Rong, D. H. Ping, F. X. Yin, Y. Y. Li, *Mater. Lett.* **2010**, *64*, 1411.
[44] A. Abbasi Aghuy, M. Zakeri, M. H. Moayed, M. Mazinani, *Corros. Sci.* **2015**, *94*, 368.
[45] Y. Zhou, D. L. Engelberg, *Metals (Basel)* **2020**, *10*, 794.
[46] N. Alonso-Falleiros, M. Magri, I. G. S. Falleiros, *Corrosion* **1999**, *55*, 769.
[47] S. Y. Lu, K. F. Yao, Y. B. Chen, M. H. Wang, X. Liu, X. Ge, *Electrochim. Acta* **2015**, *165*, 45.
[48] S. K. Bonagani, V. Bathula, V. Kain, *Corros. Sci.* **2018**, *131*, 340.
[49] M. Godec, D. A. S. Balantič, *Sci. Rep.* **2016**, *6*, 29734.
[50] F. Hu, K. M. Wu, T. P. Hou, A. A. Shirzadi, *Mater. Sci. Technol.* **2013**, *29*, 947.
[51] A. A. Salih, M. Z. Omar, J. Junaidi, Z. Sajuri, *Aust. J. Basic Appl. Sci.* **2011**, *5*, 867.

12 | **Materials and Corrosion**

ZHOU AND ENGELBERG

[52] Y. Yang, H. Zhao, H. Dong, *J. Mater. Eng. Perform.* **2020**, *29*, 3868.

[53] T. Moisio, M. Mannerkoski, *Corros. Sci.* **1969**, *9*, 129.

[54] I. Taji, M. H. Moayed, M. Mirjalili, *Corros. Sci.* **2015**, *92*, 301.

[55] M. G. Alvarez, J. R. Galvele, *Corros. Sci.* **1984**, *24*, 27.

[56] T. Q. Ansari, J.-L. Luo, S.-Q. Shi, *npj Mater. Degrad.* **2019**, *3*, 1.

[57] H. Ha, C. Taxen, K. Williams, J. Scully, *Electrochim. Acta* **2011**, *56*, 6165.

How to cite this article: Y. Zhou, D. L. Engelberg. Accessing the full spectrum of corrosion behaviour of tempered type 420 stainless steel. *Mater. Corros.* **2021**;1-12. https://doi.org/10.1002/maco.202112470